# Numerical simulation of underwater explosion cavitation characteristics based on phase transition model in compressible multicomponent fluids

Jun Yu*, Jian-hu Liu, Hai-kun Wang, Jun Wang, Lun-ping Zhang, Guo-zhen Liu
*(China Ship Scientific Research Center, Wuxi, 214082, China)*

## Abstract：

Underwater explosion cavitation has an important influence on the shock wave, explosion bubble, and structural deformation. The one-fluid model is usually used in underwater explosion cavitation. It is assumed that the cavitation is induced suddenly when the pressure is lower than the saturated pressure. The biggest deficiency of the model is that it is difficult to consider the temperature change in the cavitation domain. It is known that cavitation is sensitive to the temperature. In this paper, we study UNDEX cavitation characteristics based on the two-fluid model proposed by Chiapolino et al. (2017), which holds that the cavitation phenomenon is the result of the phase transition between the gas and liquid phases. This model is composed of the 4-equation model with phase transition relaxation, which is solved by a simple fractional step. In this article, we briefly introduce the compressible multiphase fluids model and successfully extent it to the engineering research field of underwater explosion cavitation. Through the quantitative analysis of the vapor phase content, it is suggested that the initial mass fraction of vapor phase in water should be set to less than $10^{-7}$. Meanwhile, it can be observed that the bulk cavitation near the free surface can evolve into a vortex ring until it collapses. Numerical results show that the collapsed pressure cannot be ignored relative to the shock wave in the bulk and local cavitation. Numerical results of this paper display that the phase transition model shows a great prospect of engineering application in underwater explosion cavitation.

**Keywords：**
Underwater explosion;
Compressible multicomponent fluids;
Phase transition;
Bulk cavitation;
Local cavitation;
Cavitation collapse.



* Corresponding author: Tel: +086 0510 85555246.
E-mail addresses: yujun@cssrc.com.cn; feiyue617@163.com (Jun. Yu).

## 1. Introduction

Phase transition and heat exchanges are examples of physical process appearing in many industrial applications involving multiphase compressible flows, such as ship and submarine propellers, rocket engine at ignition, and underwater explosion (UNDEX). Underwater explosion usually contains complicated sequence of the events that include detonation wave, shock wave, fluid-structure interactions and cavitation (Cole, 1948; Liu, 2006). From the published research papers on underwater explosion, there are many studies on the propagation of shock wave and the movement of explosion bubble, but the research on cavitation in underwater explosion is not enough. Cavitation can appear when an explosion occurs near water surface or structures. The pressure caused by cavitation collapse is one major concern in engineering application. The numerical model of cavitation plays an important role in the research and analysis of cavitation effect. It is helpful for understanding of the basic mechanisms that contribute to cavitation evolvement, which is one of the motivations that attract the research on cavitation flow.

Owing to the strong discontinuities such as shock wave propagation in underwater explosion, both the liquid and vapor phases in water need to be considered as compressible fluids. In multiphase compressible flows modeling, phase transition between liquid and vapor phases has important effects in these applications, and has to be accounted for via appropriate phase transition models. There are mainly two methods designed to simulate the movement mechanism in the cavitation. The first one is the one-fluid cavitation model, such as the model developed by Liu et al. (Liu et al., 2004), Qin et al. (1999) and others. This type of cavitation model treats the liquid and vapor phase using one set of governing equations considering the two phases as the same fluid. The earliest one-fluid model used extensively in underwater explosion is the Cut-off model (Aanhold et al., 1998). In this model the pressure is set to a given saturated pressure once the flow pressure is detected to be lower than the saturated pressure. However, the equation of state of water is still used for the cavitation domain, which will bring great errors to the calculation of sound speed and mixing pressure in the mixture. Liu et al. (2004) developed the isentropic one-fluid model, which assumes the fluid to be a homogeneous mixture comprising isentropic vapor and liquid phases. Schmidt model (Schmidt et al., 1999) is an important one-fluid model and can work efficiently in simulating cavitating flow occurring in high pressure and high velocity nozzles. If this model is applied to simulate the large-scale unsteady cavitation with a large vapor to liquid density ratio, however, a “saturated” pressure that is much higher than physical saturated pressure has to be employed, resulting in nonphysical large cavitation pressure or numerical oscillation on the cavitation interface. Xie et al. (2006) improved the shortcomings of Schmidt model in the simulating the unsteady transient cavitating flows with a large vapor to liquid density ratio and proposed the modified Schmidt model. Daramizadeh et al. (2015) adopted a five-equation reduced model with a new isentropic cavitation model to simulate underwater explosion cavitation near the free surface. This new model assumed the equilibrium phase’s pressure, and obtained equations of cavitation fraction and pressure parameters. The key difference between these one-fluid cavitation models is that the equation of state of the cavitation domain is different when the fluid pressure is lower than the saturated pressure.

The second method is the two-fluid cavitation model, including Le Metayer et al. (2004, 2005, 2013), Saurel et al. (2008), and Pelanti and Shyue (2014). This type of cavitation model treats the liquid and vapor phase as different fluids in the system governing equations in the whole process.

In addition to dealing with the ordinary convection between multiphase fluids, phase transition is modeled by considering thermal and chemical relaxation effects due to mass and heat conversion between liquid and vapor phase, which lead to prompt the mixture to the new desired equilibrium state. Therefore, the new relaxation source terms in phase transition system control equation associated with the heat and mass transfer appear. Chiapolino et al. (2016, 2017) proposes a simple and fast solver to compute thermodynamic equilibrium between liquid and vapor phase instead of the common iterative procedures in the 4-equation model, and allows systematic CPU saving over 50% without the cost of accuracy. Zhang (2020) adapts five-equation two-phase flow model for liquid-vapor phase transition in cavitating flows by temperature and chemical potential relaxation with the monotonic mixture speed of sound. This model is based on the volume fraction of each phase, and it is unable to deal with other fluids except liquid and vapor phase of a phase-transition fluid.

At present, one-fluid model is mainly used in underwater explosion cavitation (Daramizadeh et al., 2015; Shukla et al., 2010; Yu et al., 2021). This model belongs to phenomenological theory and cannot describe the mechanism of underwater explosion cavitation from the view of objective nature. Because it cannot realize the continuous and conservative tracking and capture of the flow distribution of each phase in cavitation domain. In order to overcome these difficulties, two-fluid cavitation model proposed by Chiapolino et al. (2016, 2017) is adopted in this paper. With the phase transition relaxation model here, the generation of cavitation during the propagation of rarefaction wave in underwater explosion can be simulated to provide a more accurate understanding on the cavitation bubble collapse. The pressure loading of cavitation collapse is important to the assessment of the destructive effects on the submarine structure. This paper is organized as follows. In Section 2, the 4-equation model with phase transition is introduced; In Section 3, the numerical method is provided to solve the system of equations; In Section 4, underwater explosion cavitation is simulated and discussed; Finally, some conclusions are made from this study.



## 2. Phase transition model based on 4-equation in multiphase compressible flows

### *2.1. Governing equations*

The governing equations for multiphase compressible flows without phase transition are (Chiapolino et al., 2017)

$$\begin{cases} \dfrac{\partial \rho}{\partial t} + \nabla \cdot \left( \rho \mathbf{u} \right) = 0 \\ \dfrac{\partial \left( \rho \mathbf{u} \right)}{\partial t} + \nabla \cdot \left( \rho \mathbf{u} \otimes \mathbf{u} + p\mathbf{I} \right) = 0 \\ \dfrac{\partial \left( \rho E \right)}{\partial t} + \nabla \cdot \left( \left( \rho E + p \right) \mathbf{u} \right) = 0 \\ \dfrac{\partial \rho Y_k}{\partial t} + \nabla \cdot \left( \rho Y_k \mathbf{u} \right) = 0 \end{cases} \tag{2.1}$$

where $\rho, \mathbf{u}, p, E$ account for the mixture density, flow velocity vector, mixture pressure and total energy per unit mass, respectively. $Y_k$ is mass fraction of the $k$-th phase fluid. The parameter $k$ here is specified as follows: $k = 1$ for the liquid phase, $k = 2$ for the gas phase corresponding to vapor of species 1, and $k = 3, \ldots, N$ for the other fluids without phase transition.

### *2.2. Equation of state*

The Noble-Abel Stiffened-Gas (NASG) equation of state is used to describe different phase flows (Le Metayer and Saurel, 2016). The main formulas for the NASG EOS read for a given phase $k = 1, \ldots, N$ are

$$\begin{cases} p_k\left(\upsilon_k, e_k\right) = \dfrac{\left(\gamma_k - 1\right)\left(e_k - q_k\right)}{\upsilon_k - b_k} - \gamma_k p_k^{\infty} \\ T_k\left(p_k, \upsilon_k\right) = \dfrac{\left(p_k + p_k^{\infty}\right)\left(\upsilon_k - b_k\right)}{\left(\gamma_k - 1\right) C_{\mathrm{v},k}} \\ g_k\left(p_k, T_k\right) = \left(\gamma_k C_{\mathrm{v},k} - q_k'\right) T_k - C_{\mathrm{v},k} T_k \ln \dfrac{T_k^{\gamma_k}}{\left(p_k + p_k^{\infty}\right)^{\gamma_k - 1}} + b_k p_k + q_k \\ c_k\left(p_k, \upsilon_k\right) = \sqrt{\dfrac{\gamma_k \upsilon_k^2 \left(p_k + p_k^{\infty}\right)}{\upsilon_k - b_k}} \end{cases} \tag{2.2}$$

Where $e$, $\upsilon = 1/\rho$, $T$, $g$, $c$ account for the internal energy, the specific volume, the temperature, the Gibbs free energy (also known as chemical potential energy) and the sound speed of the considered phase, respectively. The Gibbs free energy can be obtained by $g = h\text{-}Ts$, with $h$ and $s$ being the enthalpy and entropy, respectively. The parameters $\gamma_k, p_k^{\infty}, C_{\mathrm{v},k}, q_k, q_k', b_k$ are constant coefficients characteristic of the thermodynamic properties of the fluid. It is convenient to obtain these parameters once the saturation curves are known (Raurel et al., 2016). The formulas of specific volume, internal energy, temperature and entropy can be obtained by simple transformation of Eq. (2.2), and it is helpful for compiling the computational program.

$$\begin{cases} \upsilon_k\left(p_k, T_k\right) = \dfrac{T_k C_{\mathrm{v},k}\left(\gamma_k - 1\right)}{p_k + p_k^{\infty}} + b_k \\ e_k\left(p_k, T_k\right) = \dfrac{p_k + \gamma_k p_k^{\infty}}{p_k + p_k^{\infty}} C_{\mathrm{v},k} T_k + q_k \\ T_k\left(e_k, p_k\right) = \dfrac{\left(e_k - q_k\right)\left(p_k + p_k^{\infty}\right)}{C_{\mathrm{v},k}\left(p_k + \gamma_k p_k^{\infty}\right)} \\ s_k\left(p_k, T_k\right) = C_{\mathrm{v},k} \ln \dfrac{T_k^{\gamma_k}}{\left(p_k + p_k^{\infty}\right)^{\gamma_k - 1}} + q_k' \end{cases} \tag{2.3}$$

A formulation connecting the saturation pressure and temperature can be obtained by equating the liquid and vapor Gibbs free energy $g_1 = g_2$, leading to the following formula:

$$\ln(p_{sat} + p_2^{\infty}) = A + \frac{B + E \cdot p_{sat}}{T_{sat}} + C \cdot \ln(T_{sat}) + D \cdot \ln\left(p_{sat} + p_1^{\infty}\right) \tag{2.4}$$

with

$$A = \frac{C_{p,1} - C_{p,2} + q_2' - q_1'}{C_{p,2} - C_{v,2}},\quad B = \frac{q_1 - q_2}{C_{p,2} - C_{v,2}},\quad C = \frac{C_{p,2} - C_{p,1}}{C_{p,2} - C_{v,2}},\quad D = \frac{C_{p,1} - C_{v,1}}{C_{p,2} - C_{v,2}},\quad E = \frac{b_1 - b_2}{C_{p,2} - C_{v,2}} \tag{2.5}$$

Where $C_{p,k}$ denotes heat capacity at constant pressure to the k phase with $C_{p,k} = \gamma_k C_{\mathrm{v},k}$.

For liquid water and its vapor phases, the NASG parameters are given in Table 1 (Le Metayer and Saurel, 2016). These parameters are used in the computational examples of this paper associated with water phase transition.

| Coefficients | Liquid water | Water vapor | air |
|---|---|---|---|

| | | | |
|---|---|---|---|
| $C_p\,(\mathrm{J/kg/K})$ | 4285 | 1401 | 1007 |
| $C_v\,(\mathrm{J/kg/K})$ | 3610 | 955 | 719 |
| $\gamma$ | 1.19 | 1.47 | 1.4 |
| $P_\infty\,(\mathrm{Pa})$ | 7.028e8 | 0 | 0 |
| $q\,(\mathrm{J/kg})$ | -1177788 | 2077616 | 0 |
| $q'\,(\mathrm{J/kg/K})$ | 0 | 14317 | 0 |
| $b\,(\mathrm{m^3/kg})$ | 6.61e-4 | 0 | 0 |
| $W\,(g/\mathrm{mol})$ | 18 | 18 | 29 |

Table 1. NASG coefficients for liquid water, water vapor, and air

### *2.3. Phase transition model*

Under the conservative system (2.1), the equations of the mixture mass, mixture momentum and mixture energy are unaffected, while only mass fraction equation may be modified through phase transition relaxation process by Gibbs free energy relaxation terms (Chiapolino et al., 2017),

$$\begin{cases} \dfrac{\partial \rho Y_1}{\partial t} + \nabla \cdot \left( \rho Y_1 \mathbf{u} \right) = \rho \nu \left( g_2 - g_1 \right) \\ \dfrac{\partial \rho Y_2}{\partial t} + \nabla \cdot \left( \rho Y_2 \mathbf{u} \right) = \rho \nu \left( g_1 - g_2 \right) \end{cases} \tag{2.6}$$

Where $g_1$, $g_2$ denote Gibbs free energy for liquid and vapor phases, respectively. $v$ represents relaxation parameter that controls the rate that thermodynamic equilibrium is reached, which will be zero for locations far from the interface between liquid and vapor phases. Such procedure is described as

$$\nu = \begin{cases} +\infty & for \quad \varepsilon \le Y_2 \le 1-\varepsilon \\ 0 & others \end{cases} \tag{2.7}$$

Where $\varepsilon$ denotes a very small positive number (typically on the order of $10^{-8}$), so the inequality $\varepsilon \le Y_2 \le 1-\varepsilon$ represents the existence of both liquid and vapor phase in the mixture fluid element. At the liquid-vapor interface the relaxation parameter $\nu$ will be taken infinite in order to achieve equilibrium interface conditions with mass transfer instantly. Therefore, the system equations are solved using a simple fractional step approach that consists of the homogeneous hyperbolic system without mass and heat transfer, followed by the relaxation step through the solution of a simple system of algebraic equations for the equilibrium state variables. At each time step, the relaxation step equation corresponding to Eq. (2.6) can be expressed as

$$\frac{\partial \rho Y_1}{\partial t} = \frac{\rho \left( Y_1^* - Y_1 \right)}{\tau}; \qquad \frac{\partial \rho Y_2}{\partial t} = \frac{\rho \left( Y_2^* - Y_2 \right)}{\tau} \tag{2.8}$$

Where $Y_1^*, Y_2^*$ account for the two phases mass fraction at which thermodynamic equilibrium is reached, respectively. This equation describes the hyperbolic step solutions $(Y_1, Y_2)$ reach their

thermodynamic equilibrium values $\left(Y_1^*, Y_2^*\right)$ with a characteristic time $\tau$. Therefore, the solution of relaxation step $\left(Y_1^*, Y_2^*\right)$ are regarded as the initial value of the new time step.

During the phase transition process, the mixture specific volume $\upsilon = 1/\rho$ and internal energy $e$ do not vary under the assumption of a single pressure and a single velocity in 4-equation model. The mass fractions of phases $Y_{k\geq 3}$ also remain constant, although the pressure and temperature vary and reach their equilibrium values $\left(p^*, T^*\right)$. Therefore, the phase transition model will change to compute the equilibrium state $\left(p^*, T^*, Y_{k=1,2}\right)$ from the state $\left(\upsilon, e, p, T, Y_k\right)$ at every time step. Therefore, under the assumption of mechanical and thermal equilibrium, the mixture flow satisfies (Chiapolino et al., 2017; Zhang, 2020)

$$\begin{cases} T = T_k, & p = p_k, \quad \forall k \\ \upsilon = \sum_{k=1}^{N} Y_k \upsilon_k, & e = \sum_{k=1}^{N} Y_k e_k \end{cases} \tag{2.9}$$

These formulas are well described in the literature (Chiapolino et al., 2017). They are also outlined in the section to keep this paper as self-contained as possible.

There is an equivalence between the ideal gas mixture model that follows Dalton's partial pressure law, and a gas phase with each constituent is assumed to occupy its own volume with assumption of temperature and pressure equilibrium, which leads to

$$p = \sum_{k=2}^{N} \frac{Y_k \rho \hat{R} T}{W_k} \tag{2.10}$$

where $\rho, \hat{R}, W_k$ are the density of mixture gas, universal gas constant in molar units, and molar mass of species *k*, respectively.

Under the assumption of mechanical and thermal equilibrium, the variables of $\rho \hat{R} T$ in Eq. (2.10) is constant. Therefore, the vapor partial pressure is directly proportional to the vapor molar fraction:

$$p_{partial} = \frac{Y_2 / W_2}{\sum_{k\geq 2}\left(Y_k / W_k\right)} p \tag{2.11}$$

where $p_{partial}$ denotes the vapor partial pressure and $p$ the mixture pressure. So that the expression satisfied at thermochemical equilibrium is

$$p_{sat}\left(T^*\right) = p_{partial} = \frac{Y_2^* / W_2}{\sum_{k\geq 2}\left(Y_k^* / W_k\right)} p^* \tag{2.12}$$

Using Eq. (2.9), the equilibrium state can be described as:

$$\begin{cases} p_{partial} = \dfrac{Y_2^* / W_2}{Y_2^* / W_2 + \sum_3^N Y_k / W_k} p^* = p_{sat}\left(T^*\right) \\ \upsilon = Y_1^* \upsilon_1\left(T^*, p^*\right) + Y_2^* \upsilon_2\left(T^*, p^*\right) + \sum_{k=3}^N Y_k \upsilon_k\left(T^*, p^*\right) \\ e = Y_1^* e_1\left(T^*, p^*\right) + Y_2^* e_2\left(T^*, p^*\right) + \sum_{k=3}^N Y_k e_k\left(T^*, p^*\right) \end{cases} \tag{2.13}$$

Combining Eq. (2.4) and (2.13), there are four unknown variables $\left(p_{sat}, T^*, p^*, Y_2^*\right)$ with four equations, which is vary suitable to use an iterative method such as Newton-Raphson method. The advancing formula for a single variable is

$$q_{n+1} = q_n - \frac{f\left(q_n\right)}{f'\left(q_n\right)} \tag{2.14}$$

where $q$ denotes the unknows variable and $f'\left(q_n\right)$ partial derivative of the equation.

For the sake of simplification, this paper assumes that they are all gas phases for $k \geq 3$.In the case of other liquids appear in the phase $k \geq 3$, it is necessary to delete the liquid molar fraction term in the formula (2.10) and (2.13).

## 3. Numerical method

Following Pelanti and Shyue (2014), Chiapolino et al. (2016, 2017), and Zhang (2020), the system equations are solved using a simple fractional step method that consists of the homogeneous hyperbolic system solution step (Step 1) and follows by the relaxation step (Step 2) through the solution of a simple system of algebraic equations for the equilibrium state variables.

The homogeneous hyperbolic system (Step 1) can be solved in conservative form using the common reconstruction-and-evolve strategy within a finite volume formulation (Akturk, 2005). The reconstruction is addressed with the MUSCL-Hancock method using van Lee's slope limiter and the numerical fluxes are built by HLLC approximate Riemann solver (Toro, 1997). In this step, the choice of sound speed in the mixture is very important. The Wood speed is used earlier in multicomponent flow computation (Kapila et al., 2001; Murrone and Guillard, 2005; Tiwari et al., 2013). The non-monotonic behavior of the mixture sound speed by the Wood sound speed with respect to the volume fraction has been point out. Therefore, several monotonic mixture sound speed formulas have been created. Allaire et al. (2002) provided a monotonic speed in five-equation model. A monotonic frozen speed of sound was established for a pressure non-equilibrium six-equation model by Saurel et al. (2009). After a large number of tests by the authors, the difference between these two kinds of speed is very small.

For the relaxation step (Step 2), the relaxation ordinary differential equations are solved indirectly in the limit of stiff (instantaneous) thermal and chemical relaxation, which enforces the mechanical, thermal and chemical equilibrium conditions in the process of reaching the equilibrium state (Zhang, 2020). The final result is obtained by solving the system of algebraic equations. In general, these equations are non-linear and need to be solved numerically, for example by Newton-Raphson iterative method.

## 4. Results and discussion

*4.1. Convergence test and verification*

To verify the convergence properties of the phase transition model, a shock wave tube case is tested with different number of cells. This problem has been simulated by Chiapolino et al. (2017) using 100 cells. A two-phase mixture with initial mass fractions set to $Y_1 = 0.1$ (liquid), $Y_2 = 0.2$ (vapor) and $Y_3 = 0.7$ (air) is considered throughout the whole shock tube with an initial pressure ratio of 2 in 1 m length tube. The initial discontinuity is located at $x = 0.5$ m. The initial condition is

$$\left(\rho, u, p, Y_1, Y_2, Y_3\right) = \begin{cases} \left(1.783, 0, 2\times10^5, 0.1, 0.2, 0.7\right) & x < 0.5 \\ \left(0.936, 0, 1\times10^5, 0.1, 0.2, 0.7\right) & x \geq 0.5 \end{cases} \tag{4.1}$$

The parameters of NASG EOS for the liquid and vapor water can be found in Table 1. The fluid domain is discretized by 100, 200, and 400 cells, respectively. Fig. 1 displays the density, pressure, velocity, temperature, liquid and vapor mass fraction distribution at time $t = 1$ ms. The dashed lines represent the initial conditions. The short-dashed lines represent the solutions without phase transition (no *P*-*T*), and the thick lines represent the present relaxation algorithm (*P*-*T*) with different cells. We can notice from the plot that there is a significant difference in the calculated results with or without phase transition. Due to the consideration of the phase transition in water, the transition from liquid phase to vapor phase occurs near the right shock wave front, resulting in an increase in the mass fraction of the gas phase and a decrease in the mass fraction of the liquid phase. As a result of the phase transition, the shock wave speed and temperature on the right side decreased.

The results with 100 cells in Fig. 1 show consistency with the simulation by Chiapolino (2017) represented by the symbol of upper triangle. We can find that the calculation accuracy increases gradually with the increase of the number of cells.

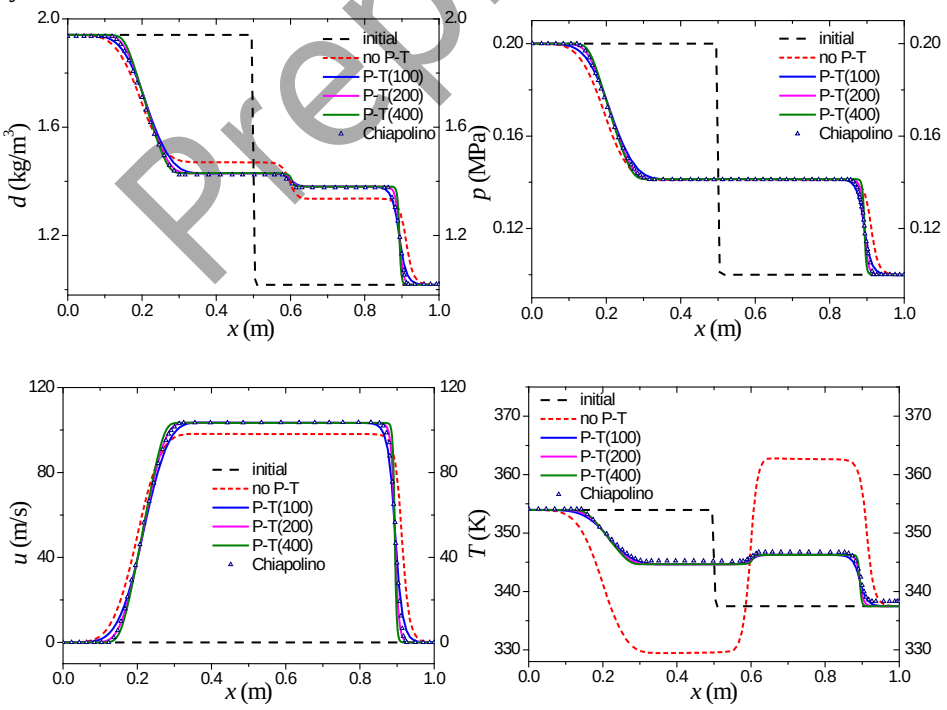

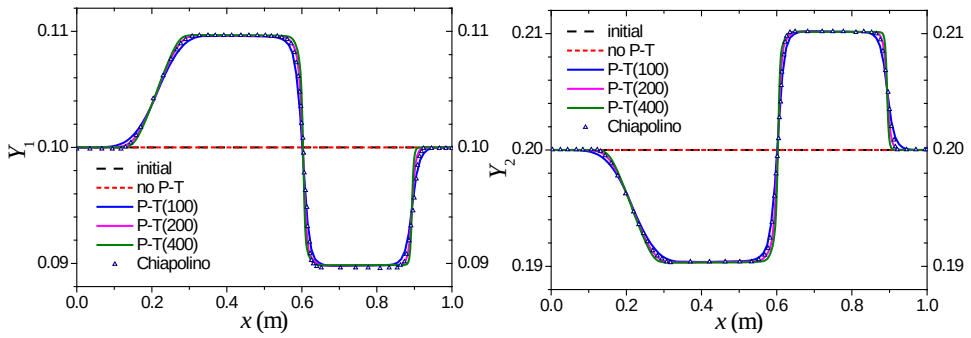


**Fig. 1.** Numerical results for shock tube test with a two-phase mixture made of liquid water, vapor water and air. The dashed lines represent the initial conditions. The short-dashed lines represent the solutions without phase transition (no *P-T*), and the thick lines represent the phase relaxation algorithm (*P-T*) with different cells.

### *4.2. Compression effect of underwater explosion shock wave on cavitation*

The interaction between the cavitation bubble and shock wave is very complicated in underwater explosion, such as the explosion near the propeller and the protection of micro-cavitation against shock wave. In order to explore the interaction mechanism between shock wave and cavitation, we analyze two kinds of problems involving shock wave impact on cavitation. The first is the direct impact of underwater explosion shock wave on a single cavitation bubble, which can be easily extend to many cavitation bubbles with different arrangement. The second is that shock wave impacts on a very small amount of cavitation initially contained in water, which can be understood as the propagation of the underwater explosion shock wave in free field. The former cavitation has an initial shape (a circle in 2D, or a sphere in 3D), while the latter has no initial shape and only has an initial uniformly distributed vapor phase mass fraction in the whole flow field. The second case has never been researched before as author's knowledge, and it is valuable to understand the propagation mechanism of underwater shock wave.

#### *4.2.1. Two-dimensional vapor bubble compression and collapse*

This example has been considered by Shukla et al. (2010), Johnsen and Colonius. (2006), Pelanti & Shyue. (2014), and Yu et al. (2020). We simulate a similar example with a stationary vapor bubble of radius 0.2 m situated at the location of (0.8, 0.6) m in a liquid-filled chamber as shown in Fig. 2. The rectangular computational domain for this problem is $\Omega =$ [0, 1.8]×[0, 1.5] m$^2$, which is discretized by 900×600 uniform grids. The initial condition is

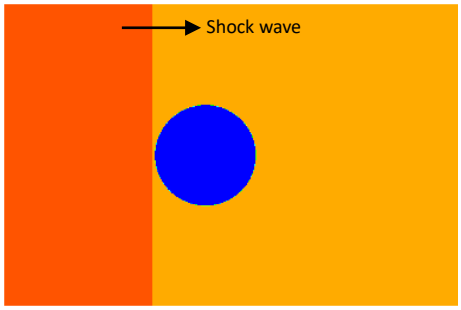


**Fig. 2.** Schematic of computation with initial cavity and compressible wave from the left

$$(\rho,u,p,Y_1,Y_2,Y_3)=\begin{cases}(1008,0,1\times10^5,0.99995,10^{-6},5.209\times10^{-5}) & x>0.6\\ (1110,275,5\times10^8,0.99998,10^{-8},1.528\times10^{-5}) & x<0.6\\ (0.61,0,1\times10^5,0.0066,0.99,3.373\times10^{-3}) & in\ \ cavity\end{cases} \tag{4.2}$$

The initial temperatures for the wave front, wave back and cavitation are set to 293, 320, and 420 K, respectively. The electronic excitation, ionization, and dissociation caused by high pressure shock wave are not considered in this paper. Numerical results with the phase transition are shown in Fig. 3. Here we provide the contour plots for the mixture density, the vapor mass fraction, temperature and mixture pressure (from left to right) at four different times $t$ = 47.6, 264.6, 350.3, and 406.2 μs (from top to bottom). Due to the left compression, the initial circular shape of the vapor bubble is deformed to a water-jet shape, which can be found from the vapor mass fraction and mixture pressure contour plots at 406.2 μs. During the compression of the spherical cavitation bubble, the temperature inside the bubble rises from 420 K at the beginning to more than 700 K and the temperature inside the bubble is non-uniformly distributed as shown in Fig. 3. Noticed that no spurious pressure oscillations at the interfaces are observed at different stages of the cavitating bubble compression, which shows that the ability of wave propagation capture and the phase transition treatment in the solver is effective.

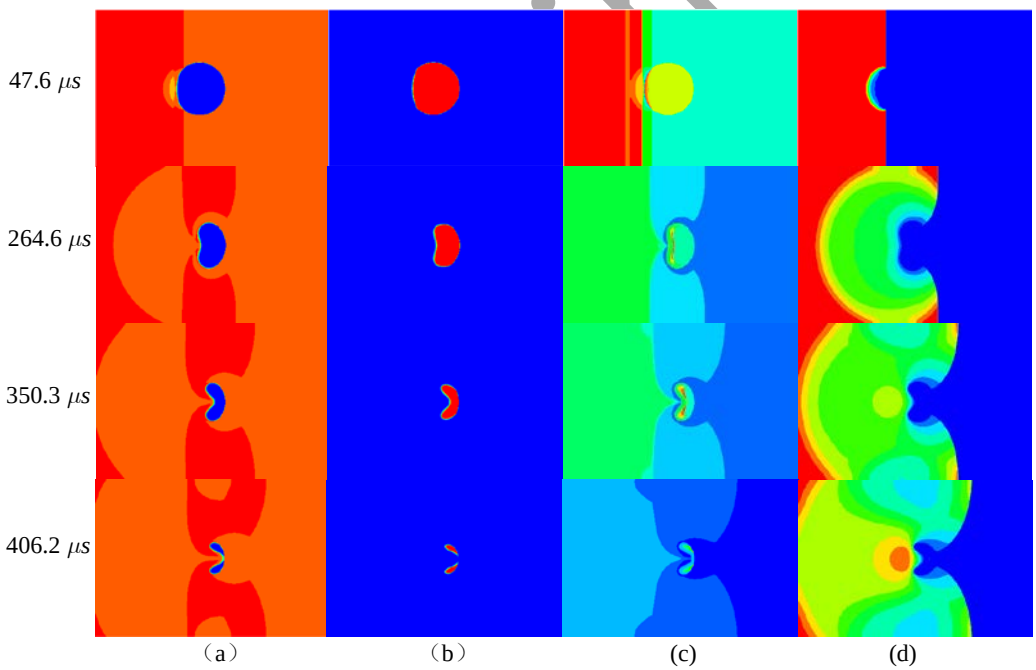


**Fig. 3.** Numerical results for the vapor-bubble compression test with phase transition model. The contour plots for (a) the mixture density; (b) vapor mass fraction; (c) temperature; (d) pressure at four different times $t$ = 47.6, 264.6, 350.3, and 406.2 μs.

*4.2.2. Compression of initial vapor phase in free water by shock wave*

Before assessing on the compression effect in water by shock wave, we need to determine the vapor phase mass fraction in water. The initial vapor phase mass fraction in ordinary water is not clearly recommended, and a weak volume fraction of vapor ($10^{-3}$) is proposed by Saurel et al.

(2008). Considering that the density of vapor phase is less than 1 kg/m$^3$ at atmospheric pressure, the mass fraction corresponding to the above volume fraction of the vapor phase is less than $10^{-5}$. In this case, we first analyze the mixture density of water at the temperature of 275, 285, 295, and 305 K under atmospheric pressure (1 atm). The curve of the relationship between the mixture density and vapor phase mass fraction at different temperatures in ordinary water is shown in Fig. 4. The liquid, vapor and air phase in water are all in saturated state in Fig. 4. We can find that the mixture density of water decreases with the increase of vapor phase mass fraction. As is known that the density of water is about 1000 kg/m$^3$ at atmospheric pressure. Noticed that the mixture density of water in saturated state is much less than 1000 kg/m$^3$ when the vapor phase mass fraction is greater than $10^{-6}$. Therefore, we recommend that the vapor phase mass fraction in water should be set less than $10^{-6}$ in numerical computation.

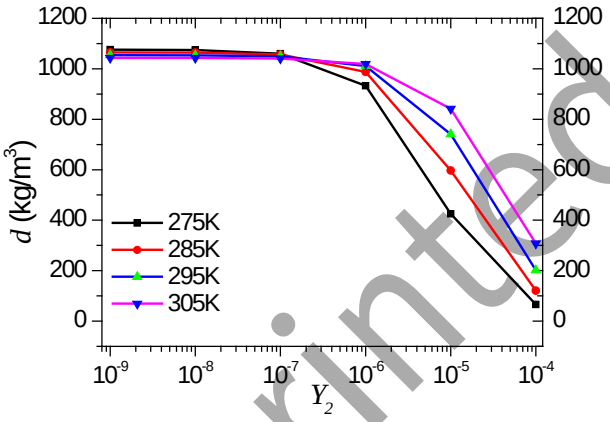


**Fig. 4.** The relationship between the mixture density and vapor phase mass fraction at different temperatures in free water

In order to research the compression of initial vapor phase by shock wave in underwater free field, 1D model is used. In this section, the tube is 1m long, and the initial discontinuity is located at 0.5 m. The left fluid is high-pressure gas and the right is water. The left boundary is set symmetric condition and the right boundary is set transmission condition. This case is used to simulate the shock wave impact on the water with initial trace vacuoles, while the vapor phase mass fraction in water is in the range of $10^{-9}$~$10^{-6}$. The initial conditions with vapor phase mass fraction $10^{-7}$ can be shown as follow

$$\left(\rho, u, p, Y_1, Y_2, Y_3\right) = \begin{cases} \left(1380.4, 0, 4.29\times10^8, 0, 10^{-3}, 0.999\right) & x < 0.5 \\ \left(1049.4, 0, 10^5, 0.999, 10^{-7}, 4.58\times10^{-6}\right) & x \geq 0.5 \end{cases} \tag{4.3}$$

The initial temperatures for left explosive gas and right water are set to 1080 and 295 K, respectively, while the gas is overheated and the water is saturated. The fluid domain is discretized by 400 cells. Fig. 5 displays the density, pressure, velocity, temperature, liquid and vapor mass fraction distribution under the condition of different vapor phase mass fraction mentioned above at time $t$ = 0.2 ms. The case of both explosive gas and water without vapor phase are also added as a comparison (as depicted by "*no vap*" in the figure).

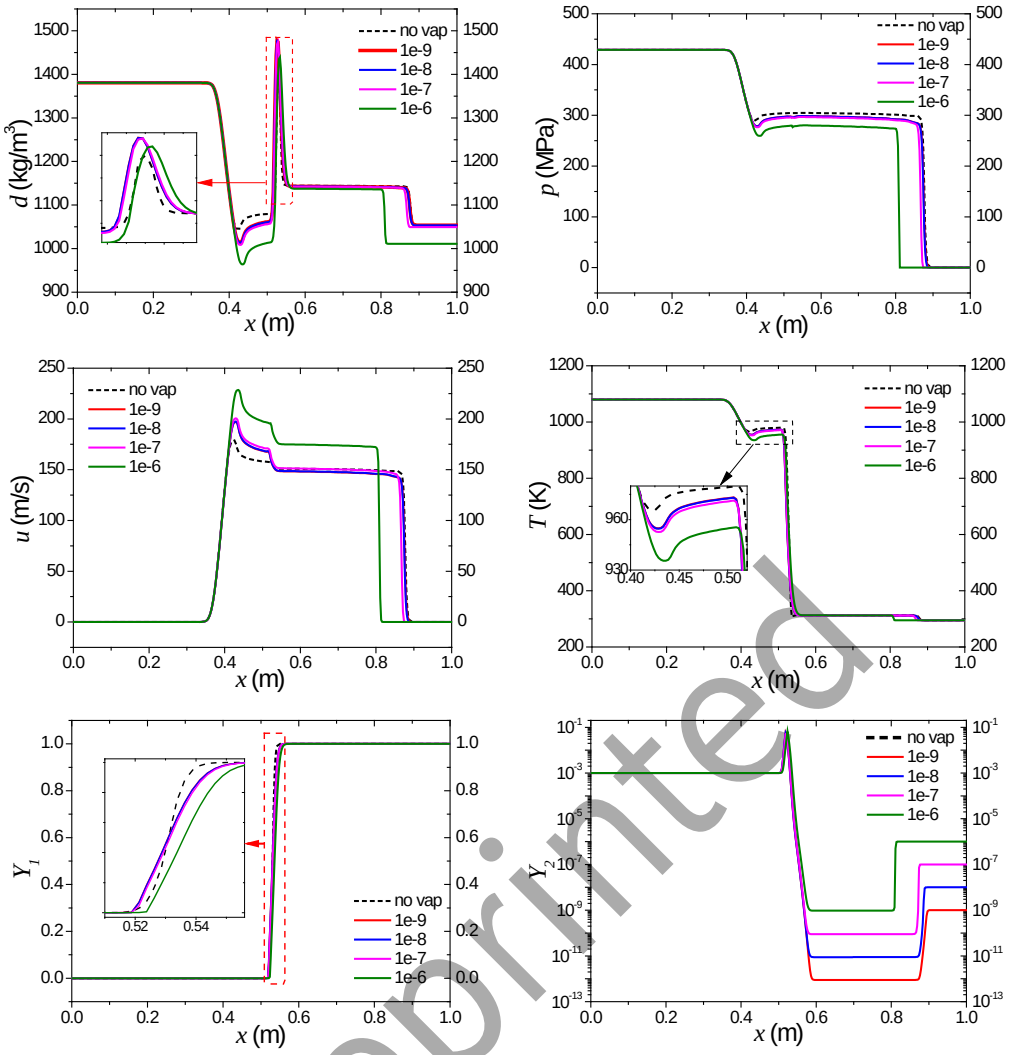


**Fig. 5.** Numerical results for shock wave compression on initial cavitation under different vapor mass fraction in water at $t$ = 0.2 ms. (The "no vap" case in the last picture is zero everywhere and cannot be displayed in logarithmic coordinate)



Fig. 5 shows that the explosive gas on the left compresses the right water, which causes the shock wave to propagate in the water. During the propagation of shock wave in water, a relatively stable domain will be formed behind the wave front. Under the impact of shock wave, the temperature of water increases from 295 to 312.6 K, and the vapor phase mass fraction decreases by about 3 orders of magnitude on average shown in Fig. 5.

Because a very small number of cavitation bubbles in water cannot be geometrically modeled separately, it is described based on statistical averages. It can be observed that the temperature increases, and the vapor mass fraction in water decreases after the compression of shock wave. By comparing the results under different vapor mass fraction in Fig. 5, it is suggested that the vapor mass fraction in numerical computation should be set to less than $10^{-7}$.

*4.3. The bulk cavitation near free surface in underwater explosion*

A two-dimensional axisymmetric model is used to simulate the cavitation phenomenon in underwater explosion near free surface. The rectangular computational domain for this problem is

$\Omega$=[0, 1.5]×[0, 2] m$^2$, which is discretized by 600×800 uniform grids as shown in Fig. 6. The spherical explosive gas has a radius of $R0$ = 0.03 m and is placed at $L0$ = 0.2 m under water surface. The thickness of air layer is 0.3 m, and the water depth is 1.7 m. The left boundary (y-axis) of the computational domain is set to the symmetry condition, and the other three boundaries are set to the transmission condition. The initial condition is

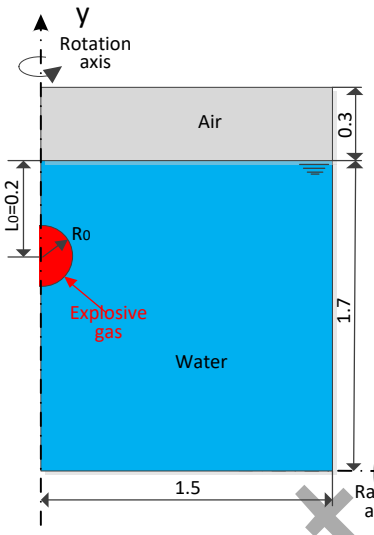


**Fig. 6.** Schematic of underwater explosion near free surface

$$(\rho,u,p,Y_1,Y_2,Y_3)=\begin{cases}(1.18,0,10^5,0,10^{-9},0.999) & \text{for } air\\ (1054,0,10^5,0.999,10^{-8},4.73\times10^{-7}) & \text{for } water\\ (1343.5,0,4.29\times10^8,0,0.05,0.95) & \text{for } gas\end{cases} \tag{4.5}$$

The initial temperatures for air, water and explosive gas are set to 295, 295, and 1080 K, respectively, while the air and explosive gas are overheated and the water is saturated. Numerical results are provided by the contours of the density, pressure, vapor volume fraction, and cavitation domain at four different times $t$ = 0.20, 0.31, 0.64, and 1.08 ms as shown in Fig. 7. The coordinate range of all the observation windows in Fig. 7 is [-1, 1]×[0.5, 2] m$^2$. Here, we define the element in which the vapor volume fraction in water is greater than 0.0005 ($\phi_2$ > 0.0005) as the cavitation domain, excluding the element above free surface and near the explosion bubble interface that meet the condition. Since there is no exact criterion for judging the vapor phase content in the cavitation domain visible to the naked eye, the above definition is only a reference value and still needs to be further studied based on experimental results. Fig. 7 shows the typical moment of cavitation evolvement after the propagation of the underwater explosion shock wave impacts on the water surface. As the shock wave reaches the free surface, rarefaction wave is reflected and results in a sharp drop in pressure in the fluid. The saturated temperature corresponding to the falling liquid pressure decreases a lot, but the actual temperature in the area does not drop much, which induces the domain to be overheated. Therefore, it can be observed that the vapor volume fraction increases greatly and a low-pressure area appears as shown at 0.2 ms in Fig. 7. When the explosion bubble moves upward, the cavitation domain on the y-axis is compressed and begins to

deform. The cavitation domain begins to expand outward to form a vortex ring (from the two-dimensional axisymmetric model) at 0.31, 0.64 and 1.08 ms.

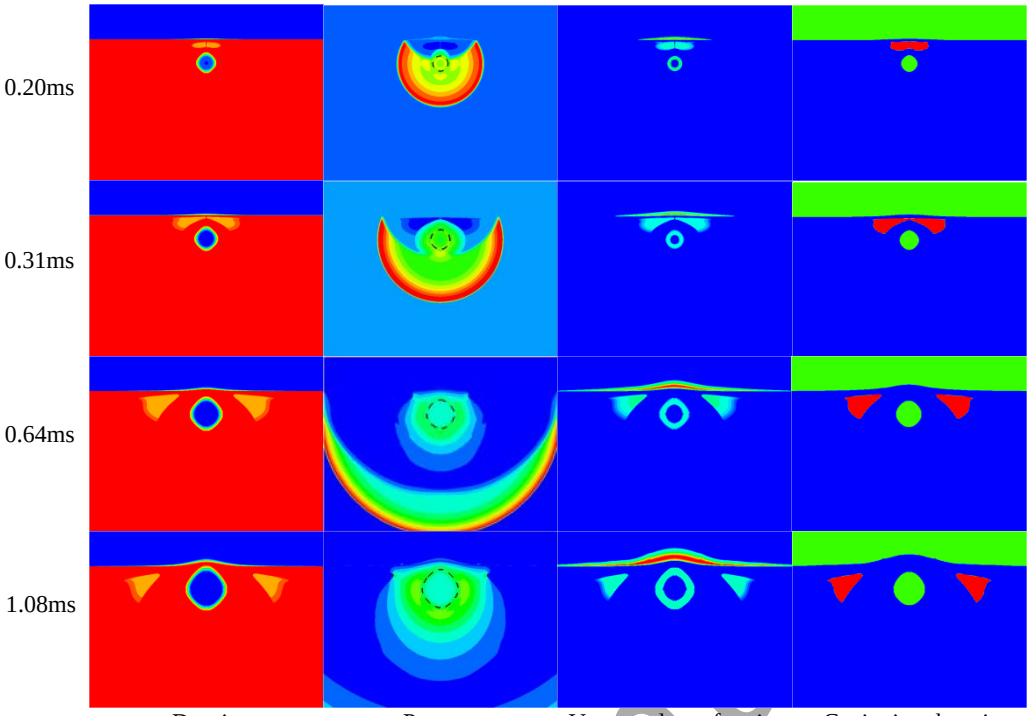


**Fig. 7.** Numerical results for underwater explosion cavitation near free surface with phase transition model. The contour plots for the density, pressure, vapor volume fraction, and cavitation domain at times $t$ = 0.20, 0.31, 0.64, and 1.08 ms. The black dotted lines in the pressure contour plots represent the general locations of explosion bubble interface, and the red region in the cavitation domain contour plots represent the locations of cavitation in water.



We set up several pressure measuring points on the axisymmetric axis ($y$-axis) at different vertical distance from the water surface. Fig. 8 shows the pressure time history curves at these points. The shock wave pressure is reduced sharply during the period of cavitation and the collapsed pressure is very obvious. It can be observed that when the distance between the measured point and the free surface is closer, the peak value of collapsed pressure is smaller. The peak values of cavitation collapsed pressure are 5.13, 5.84, 5.96, and 7.58 MPa, respectively. Meanwhile, it can be seen that the cavitation collapsed pressure at the closet measured point from the free surface rises later than others as shown in Fig. 8. This phenomenon can be explained from the evolvement of pressure contour plots in Fig. 7. The cavitation domain on the y-axis begins to be compressed by the high-pressure region directly below at 0.20 ms, and the cavitation begins to collapse gradually to produce water-hammer pressure. The high-pressure region comes from two aspects. Firstly, after the shock wave is reflected into a rarefaction wave on the water surface, the rarefaction wave propagates downward and then reflects into a compression wave when it reaches the explosion bubble interface. Secondly, during the expansion of the explosion bubble, it will have a certain compression effect on the upper fluid. Although the measuring point closest to the free surface is the earliest to produce cavitation due to the reflected rarefaction wave, it collapses at the latest.

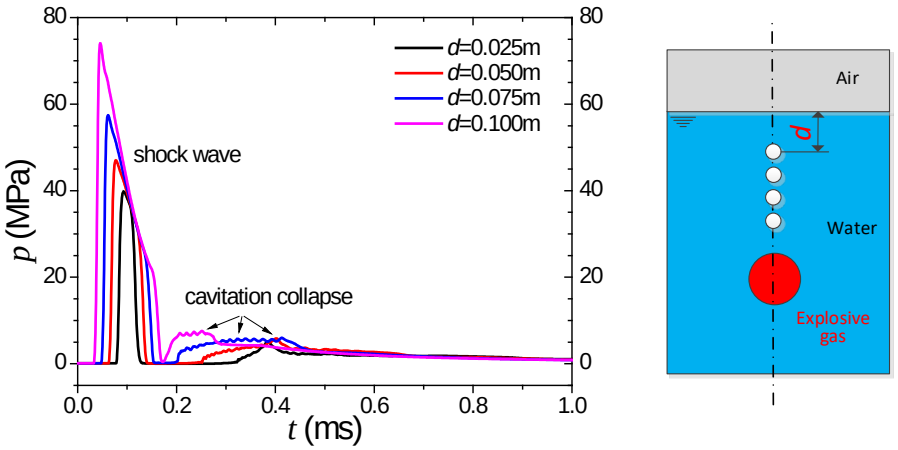


**Fig. 8.** Pressure time-history curves for different vertical distance from the initial water surface on the axisymmetric axis (left) and schematic diagram of measuring point location (right).

Fig. 9 shows the pressure time history curves of different horizontal distance from the center of explosive gas at a depth of 0.05 m. When the cavitation domain moves outward as shown in Fig. 7, the collapsed pressure gradually propagate to these horizontal measuring points. The peak values of these five points are 4.95, 2.88, 2.21, 1.85, and 2.60 MPa, respectively from the horizontal distance of 0.063, 0.125, 0.188, 0.250, and 0.313 m as shown in the right schematic diagram of Fig. 9. It can be seen that the effective loading time of cavitation collapsed pressure is much longer than that of the shock wave at the same measuring point.

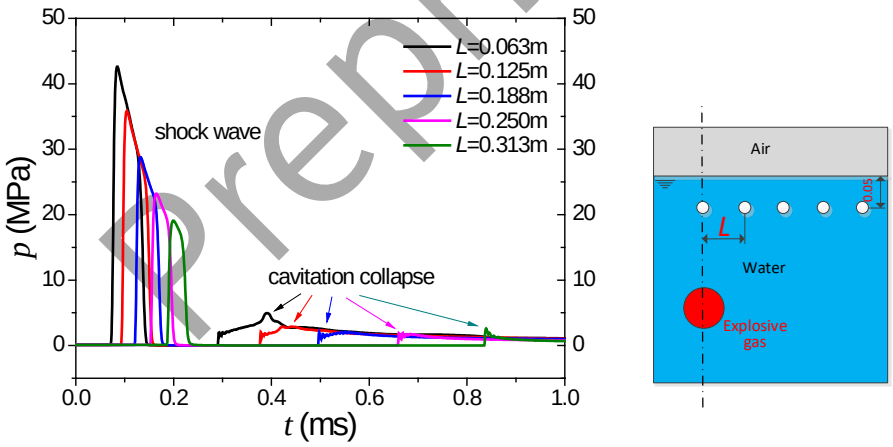


**Fig. 9.** Pressure time-history curves for different horizontal distance from explosive gas at a depth of 0.05 m (left) and schematic diagram of measuring point location (right).



*4.4. The local cavitation near solid wall in underwater explosion*

The local cavitation can be induced by the movement of structures and effect of the explosion bubble interface. In this section, the interaction between of the structure and flow is ignored in the local cavitation, and the structure is replaced by the solid wall. According to our experience, it is difficult to produce local cavitation in three-dimensional near-wall underwater explosion if we only rely on the effect of the explosion bubble interface. Because the shock wave attenuates rapidly in three-dimensional space, the reflective rarefaction wave from the explosion bubble

interface is very weak and difficult to reach the condition of cavitation. Next, we will analyze the local cavitation effect in one-dimensional and two-dimensional models, respectively.

*4.4.1. One-dimensional local cavitation model*

The first case is the one-dimensional underwater explosion as shown in Fig. 10. The length of explosive gas is 0.2 m with a distance of 0.5 m from the solid wall on the left. The computation domain for this problem is 2 m and discretized by 400 cells. The left and right boundary are fixed and transmitted conditions, respectively. The initial condition is

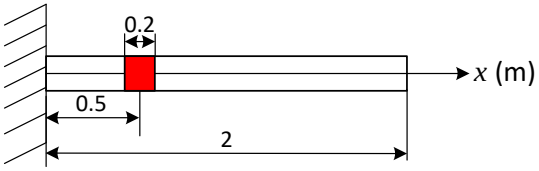


**Fig. 10.** Schematic of one-dimensional local cavitation model near the solid wall

$$(\rho, u, p, Y_1, Y_2, Y_3) = \begin{cases} (1054, 0, 10^5, 0.999, 10^{-8}, 4.73\times10^{-7}) & \text{for } water \\ (1343.5, 0, 4.29\times10^8, 0, 0.05, 0.95) & \text{for } gas \end{cases} \tag{4.6}$$

Fig. 11 shows the time history of pressure measuring points at different locations. It can be observed that the initial shock wave is reflected by solid wall, and the rarefaction wave will appear when the former reflective wave reaches explosion bubble interface. Due to the slow attenuation of shock wave in one-dimensional model and the reflection effect of solid wall, the peak pressure of local cavitation collapse is very large, which is almost equal to the peak pressure of shock wave at same measuring point in free field condition without wall reflection effect.

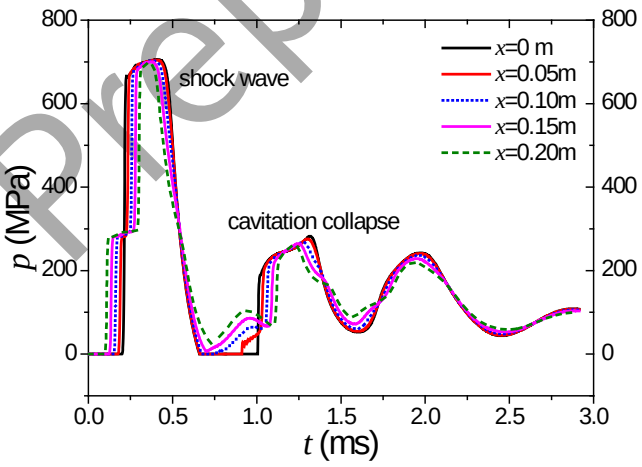


**Fig. 11.** Pressure time-history curves of different measuring points on x-axis

*4.4.2. Two-dimensional local cavitation model*

We now perform a 2D example as shown in Pelanti and Shyue (2019), and make some comparison and discussion under the same initial conditions between the two models. A cylindrical underwater explosion (UNDEX) is simulated near a rigid wall as shown in Fig. 12. An initial gas is surrounded by liquid water and located near an upper rigid wall. The computational domain is $\Omega$ = [-0.6, 0.6] × [-0.7, 0] m$^2$, which is discretized by 480 × 280 uniform grids. The gas

bubble is located at (0, -0.22) m with a radius of 0.05 m. An ideal gas law is used for the explosion gas with $\gamma = 2$.

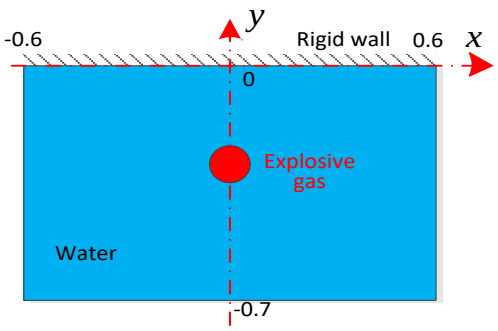


**Fig. 12.** Schematic of underwater explosion near a rigid wall.

The initial condition is

$$(\rho, u, p, Y_1, Y_2, Y_3) = \begin{cases} (1050, 0, 10^5, 0.9999, 10^{-8}, 4.73\times10^{-7}) & \text{for } water \\ (1400, 0, 8.29\times10^8, 0, 10^{-8}, 0.999) & \text{for } gas \end{cases} \tag{4.7}$$

The initial temperature of water and explosion gas is set as 295 and 827 K. Fig. 13 shows the contours of the density, pressure, vapor volume fraction, and cavitation domain at times $t$ = 0.2, 0.325, 0.406, and 0.5 ms. The identification criterion of the cavitation domain is the same as that in Fig. 7, and the coordinate range of all the observation windows in Fig. 13 is [-0.6, 0.6] × [-0.7, 0] m$^2$. The black dotted lines indicate the general location of explosion bubble interface, and the red regions represent cavitation domain in water. It can be observed that the shock waves reflected from the upper rigid wall have reached the explosion bubble interface, and a small number of rarefaction waves have been reflected into the water at $t$ = 0.2 ms. Meanwhile, the vapor volume fraction in the liquid water near the upper interface of the explosion bubble increases significantly. With the continuous reflection of the shock wave on the upper interface of the explosion bubble, the rarefaction wave in the near water fluid increases gradually, and the rarefaction wave region expands gradually. However, the rarefaction wave reflected directly for the first time are still not enough to induce cavitation occurrence in water. The cavitation did not occur until the rarefaction wave is reflected again on the wall as shown at $t$ = 0.325 ms in Fig. 13. At $t$ = 0.406 ms, the rarefaction wave reflected from the rigid wall weakens gradually, and its region expands to the left and right sides. At the same time, the rarefaction wave reaches the upper interface of explosion bubble and reflects into a compression wave, which has a certain compression effect on the cavitation domain. Therefore, it can be observed that the cavitation domain area becomes smaller and thinner. At $t$ = 0.5 ms, the cavitation in the middle region almost completely collapses as shown in Fig. 13.

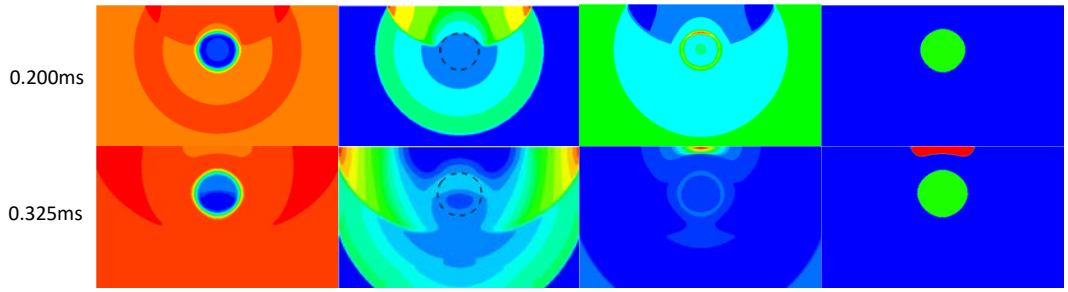

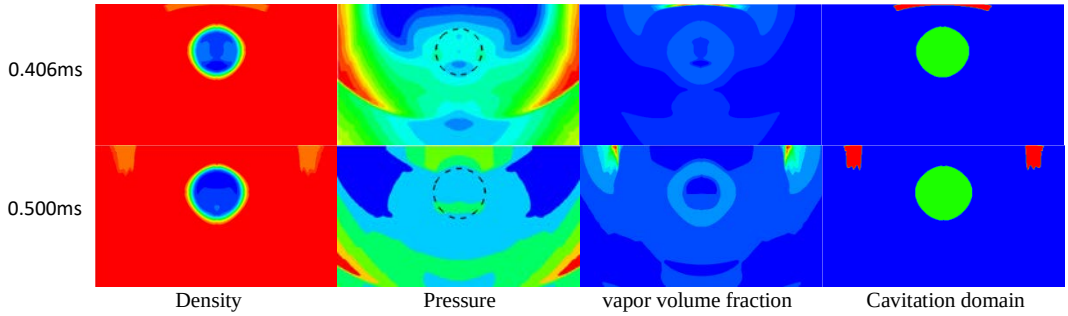


**Fig. 13.** Numerical results for underwater explosion cavitation near a rigid wall surface with phase transition model. Pseudo-color plots of the pressure, vapor volume fraction, and cavitation domain (from left to right) at four different times t = 0.200, 0.325, 0.406, and 0.500 ms (from top to bottom). The black dotted lines indicate the general location of explosion bubble interface, and the red regions represent cavitation domain in water.

Fig. 14 shows the numerical pressure time-history curves for three points on the y-axis with and without phase transition. It can be observed that the measuring point ($H$ = 0 cm) on the rigid wall is the first to produce cavitation at $t$ = 0.261 ms, which is consistent with the above conclusion that the direct rarefaction wave reflected directly for the first time cannot induce cavitation domain occurrence and needs to be further reflected and enhanced on the rigid wall. The measuring point ($H$ = 5 cm) farthest from the rigid wall begins to produce cavitation at $t$ = 0.273 ms, but its cavitation is the first to collapse. As mentioned before, the reflected compression wave from the explosion bubble interface is the first to arrive at the measuring point ($H$ = 5 cm), and the cavitation is compressed and collapses. Similar to the underwater explosion near a free surface, the phase transition has almost no effect on the early shock wave stage, but the effect on the cavitation stage is obvious and cannot be ignored. Fig. 15 shows the numerical pressure time-history curves for three points at a depth of 0.05 m with and without phase transition. It can be observed that the phase transition has a certain influence on these points in the cavitation collapse stage, but has no effect on the early shock wave stage.



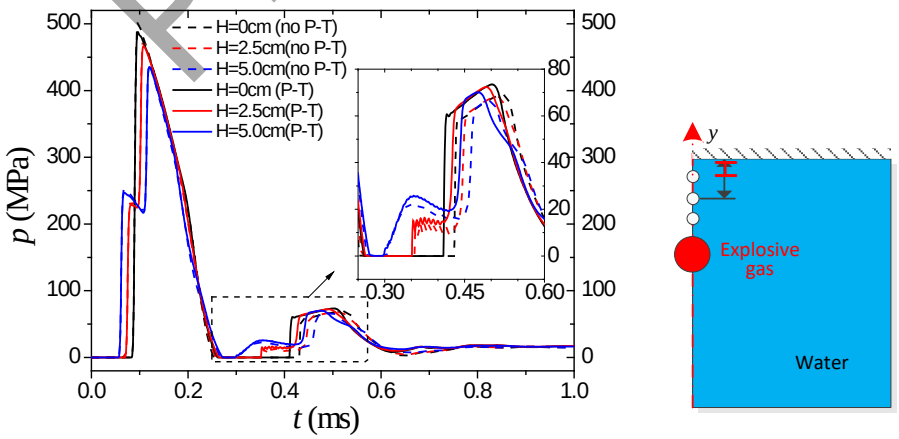


**Fig. 14.** Numerical results of the pressure time-history curves for different vertical distance from the rigid wall on the axisymmetric axis (left) and the schematic diagram of measuring point location (right).

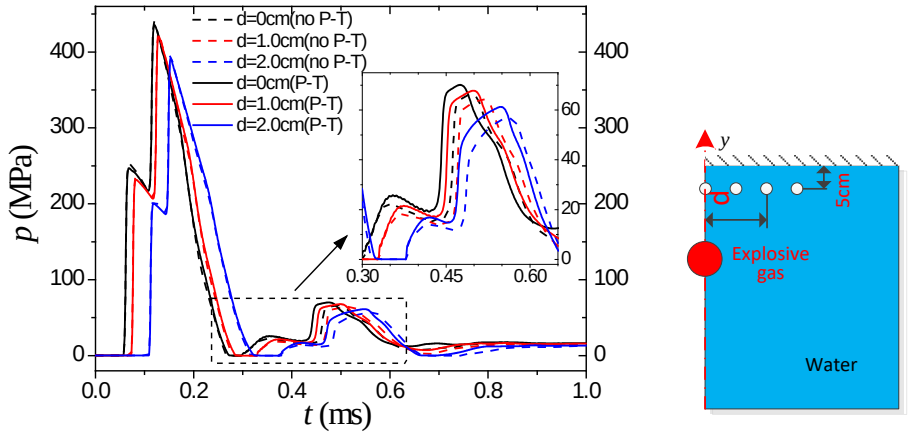


**Fig. 15.** Numerical results of the pressure time-history curves for different horizontal distance from explosive gas at a depth of 5cm (left) and the schematic diagram of measuring point location (right).

Fig. 16 shows comparison between the present and Pelanti model on the time history of the pressure, vapor volume and mass fraction with/without phase transition on the point (0, 0) m at the center of the rigid wall. In both models, phase transition has no effect on the early shock wave. It can be observed from the pressure curves that the shock wave speed in present model is higher than that of Pelanti model, which is due to the different method of the mixture sound speed. The phase transition only affects the internal pressure of the cavitation domain, but has no effect on the collapsed pressure in Pelanti model. The phase transition effect in the present model not only increase the pressure in cavitation, but also causes the cavitation to collapse 0.02 ms in advance, but has little effect on the peak value and trend of the collapsed pressure. It can be observed that the peak pressure of cavitation collapse obtained by the present model is 73.47 MPa, which is 59.2% higher than the 46.15 MPa of the Pelanti model. However, the maximum mass fraction and volume fraction of the vapor phase obtained by the present model are only about 10% of that of the Pelanti's model under the condition of phase transition. The key difference between the two models lies in the equation of state for the liquid and vapor phases and the treatment of mass and transfer in the mixture fluids. Both numerical models need to be verified by experimental results in future.



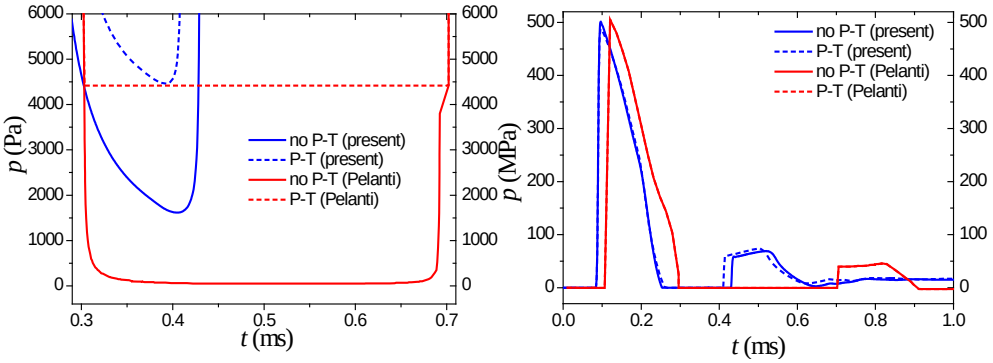

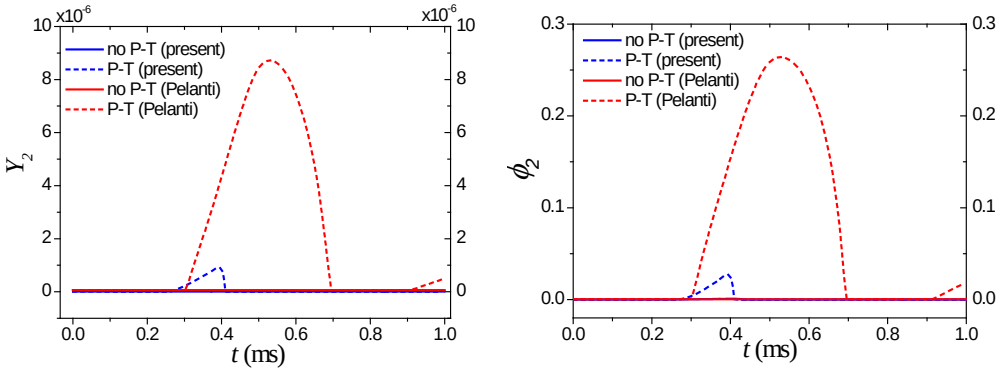


**Fig. 16.** Comparison of the present and Pelanti's model on the time history of the pressure, vapor volume and mass fraction with/without phase transition on the point (0, 0) m at the center of the rigid wall.

## 4. Conclusions

In this study, the 4-equation model with phase transition relaxation method has been introduced. The system equations are solved by a simple fractional step approach that contains hyperbolic and relaxation step. A MUSCL-Hancock method with HLLC approximate Riemann solver is applied to discretize the homogenous hyperbolic equations in hyperbolic step, and the nonlinear system is solved by Newton iterative method in the following relaxation step. The following conclusions can be drawn from this study:

(1) It can be observed that the cavitation model based on the theory of phase transition in thermodynamics shows great potential in underwater explosion. Cavitation is not simply caused by the fact that the pressure is lower than the given saturated pressure, but is closely related to several thermodynamic state quantities of the flow field (such as pressure, temperature, internal energy, etc.). Vaporization and evaporation between liquid and gas phases may occur simultaneously in underwater explosion. The phase transition model can provide a new tool for exploring and revealing the mechanism and characteristic of cavitation in underwater explosion.

(2) The initial vapor phase mass fraction contained in free water is quantitatively analyzed by the phase transition model, and the suggested value ($<10^{-7}$) is obtained in the field of numerical simulation. If the cavitation is researched from the viewpoint of phase transition, the initial vapor phase mass fraction value is important and meaningful.

(3) Considering the bulk cavitation near water surface in underwater explosion, the cavitation domain will evolve into a vortex ring until it collapses. It can be observed that when the distance between the measured point and the free surface is closer, the peak value of collapsed pressure is smaller. The cavitation collapsed pressure at the closet measured point on y-axis rises later than others, which is the result of the joint action of upward movement of explosion bubble and the compression wave reflected from the explosion bubble by the rarefaction wave.

(4) The collapsed pressure cannot be ignored relative to the shock wave load in both of the bulk and local cavitation. The influence of cavitation effect should be fully considered in the process of impact damage assessment of underwater structures, which will be finished in future research.

## References


Aanhold, J.E., Meijer, G.J., Lemmen, PPM., 1998. Underwater shock response analysis on a floating vessel, Shock Vibrat. 5, 53-59.

Akturk. A., 2005. Two dimensional finite volume weighted essentially non-osciliatory Euler schemes with different flux algorithms, The Degree of Master's thesis of Middle East Technical University.

Allaire, G., Clerc, S., Kokh, S., 2002. A five-equation model for the simulation of interfaces between compressible fluids, J. Comput. Phys. 181, 577-616.

Chiapolino. A., Boivin, P., Saurel, R., 2016. A simple phase transition relaxation solver for liquid–vapor flows, International Journal for Numerical Methods in Fluids. 83 (7), 583-605.

Chiapolino. A., Boivin, P., Saurel, R., 2017. A simple and fast phase transition relaxation solver for compressible multicomponent two-phase flows, Computers & Fluids. 150, 31-45.

Cole. R.H., 1948. Underwater explosion, New Jersey: Princeton University Press.

Daramizadeh. A, Ansari, M.R., 2015. Numerical simulation of underwater explosion near air-water free surface using a five-equation reduced model, Ocean Engineering. 110, 25-35.

Johnsen, E., Colonius, T., 2006. Implementation of WENO schemes in compressible multicomponent flow problems, J. Comput. Phys. 219,715-732.

Kapila. A., Menikoff, R., Bdzil, J.B., Son, S.F., Stewart, D., 2001. Two-phase modeling of deflagration to detonation transition in granular materials: Reduced equations, Phys. Fluids. 13, 3002-3024.

Le Metayer. O., Massoni, J., Saurel, R., 2004. Elaborating equations of state of a liquid and its vapor for two-phase flow models, Int. J. Therm. Sci. 43, 265-276.

Le. Metayer. O., Massoni, J., Saurel, R., 2005. Modeling evaporation fronts with reactive Riemann solvers, J. Comput. Phys. 205, 567-610.

Le. Metayer. O., Massoni, J. Saurel, R., 2013. Dynamic relaxation processes in compressible multiphase flows, Application to evaporation phenomena. ESAIM Proc. 40,103-123.

Le M´etayer. O., Saurel, R., 2016. The Noble-Abel Stiffened-Gas equation of state, Physics of Fluids. 28 (4), 046102.

Liu, J.H., 2002. Theory and its applications of ship dynamic responses to non-contact underwater explosions. wuxi. China. CSSRC doctor's thesis.

Liu, T.G., Khoo, B.C., Xie, W.F., 2004. Isentropic one-fluid modelling of unsteady cavitating flow, J Comp Phys. 201, 80-108.

Murrone. A., Guillard, H., 2005. A five-equation reduced model for compressible two-phase flow problems, J. Comput. Phys. 202, 664-698.

Pelanti. M., Shyue, K.M., 2014. A mixture-energy-consistent six-equation two-phase numerical model for fluid with interfaces, cavitation and evaporation waves, J. Comput. Phys. 259, 331-357.

Pelanti. M., Shyue. K.M., 2019. A numerical model for multiphase liquid-vapor-gas flows with interfaces and cavitation, Int. J. Multiphase Flow. 113, 208-230.

Qin, J.R., Yu, STJ., Lai, M.-C., 1999. Direct calculations of cavitating flows in fuel delivery pipe by the Space-Time CE/SE method, Society of Automotive Engineer. 01-3554.

Saurel. R., Boivin, P., LeMetayer, O., 2016. A general formulation for cavitating, boiling and evaporating flows, Comput. Fluids. 128, 53-64.

Saurel. R., Petitpas, F., Abgrall, R., 2008. Modelling phase transition in metastable liquids: application to cavitating and flashing flows, J. Fluid Mech. 607, 313-350.

Saurel, R., Petitpas, F., Berry, R.A., 2009. Simple and efficient relaxation methods for interfaces separating compressible fluids, cavitating flows and shocks in multiphase mixture, J. Comput. Phys. 228, 1678-1712.

Schmidt, D.P., Rutland, C.J., Corradini, M.L., 1999. A fully compressible, two-dimensional model of small, high speed, cavitating nozzles, Atomiz Sprays. 9, 255-276.

Shukla.R.K., Pantano, C., Freund, J.B., 2010. An interface capturing method for the simulation of multi-phase compressible flows, J. Comput. Phys. 229, 7411-7439.

Tiwari. A., Freund, J.B., Pantano, C., 2013. A diffuse interface model with immiscibility preservation, J. Comput. Phys. 252, 290-309.

Toro. E.F., 1997. Riemann Solvers and Numerical Methods for Fluid Dynamics, Springer, Berlin.

Xie, W.F., Liu, T.G., Khoo, B.C., 2006. Application of a one-fluid model for large scale homogeneous unsteady cavitation: The modified Schmidt model, Computers & Fluids. 35, 1177-1192.

Yu. J., G.Z. Liu, J. Wang, H.K. Wang, An effective method for modeling the load of bubble jet in underwater explosion near the wall, Ocean Engineering. 220 (2021).

Zhang. J., 2020. A simple and effective five-equation two-phase numerical model for liquid-vapor phase transition in cavitating flows, International Journal of Multiphase Flow. 132, 103417.

Pelanti. M., Shyue. K.M., 2019. A numerical model for multiphase liquid-vapor-gas flows with interfaces and cavitation, Int. J. Multiphase Flow. 113, 208-230.